Electrochimica Acta 300 (2019) 363–372

Contents lists available at ScienceDirect

Electrochimica Acta

journal homepage: www.elsevier.com/locate/electacta

Nanoporous GeO_2/Cu/Cu_2O network synthesized by dealloying method for stable Li-ion storage

Zhifeng Wang [a, b], Xiaomin Zhang [a], Yonghui Yan [a], Yongguang Zhang [a, *], Yichao Wang [c], Chunling Qin [a, **], Zhumabay Bakenov [d]

[a] School of Materials Science and Engineering, Hebei University of Technology, Tianjin, 300130, China
[b] Key Laboratory for New Type of Functional Materials in Hebei Province, Hebei University of Technology, Tianjin, 300130, China
[c] School of Life and Environmental Sciences, Deakin University, Waurn Ponds, VIC, 3216, Australia
[d] Institute of Batteries LLC, School of Engineering, National Laboratory Astana, Nazarbayev University, 53 Kabanbay Batyr Avenue, Astana, 010000, Kazakhstan

ARTICLE INFO

Article history:
Received 7 November 2018
Received in revised form
28 December 2018
Accepted 22 January 2019
Available online 25 January 2019

Keywords:
Dealloying
Nanoporous
Cu_2O
GeO_2
Li-ion battery

ABSTRACT

Transition metal oxide Cu_2O anode is still not meeting the current market demands due to the low theoretical capacity and poor cycle stability. We herein report the synthesis of a nanoporous GeO_2/Cu/Cu_2O network by a straightforward dealloying method. The resulting material possesses high porosity which served to alleviate the stress incurred during lithiation/delithiation volume variation and presents good conductivity for fast electron transfer. Enhanced electrochemical performance is observed when measured as an anode material, delivering 715 mAh g^{-1} at 200 mA g^{-1} after 50 cycles and offered 504 mAh g^{-1} even at a high current density of 1600 mA g^{-1} after 150 cycles. Furthermore, the material also demonstrates excellent rate performance of 812, 782, 741, 695, 635 and 552 mAh g^{-1} at 100, 200, 500, 800, 1600 and 3200 mA g^{-1} current densities, respectively. The enhanced Li storage performances could be ascribed to the reticular ligament with high porosity, the increased conductivity by Cu as well as the improved capacity from GeO_2. Moreover, this work provides us a new material design strategy to fabricate various porous composite anodes with high capacity through a straightforward dealloying method in future for lithium-ion battery applications.

1. Introduction

With the rapid recent technological development, various electric vehicles and electronic devices have high requirements for the capacity, energy densities and cyclic performance of lithium-ion (Li-ion) batteries [1–6]. Traditional graphite anodes, however, possess a theoretical capacity of 372 mAh g^{-1} [7], which is too low to meet the increasing market demands. So the design and exploitation of new anode materials with high capacities is urgently needed. Due to the high theoretical capacities [7,8], the alloy-typed anodes including Si and Ge materials have been focused on by many researchers. One fatal problem of these anodes is huge volume change (>300%) during discharge/charge cycling, inducing pulverization and fall off of active materials, and further resulting in fast fading in capacity. Metal oxides such as Co_3O_4, $CoFe_2O_4$, Fe_3O_4 and NiO, as one more important class of anode materials [9–12], are found to show reduced volume change rates compared with Si and Ge, and present improved theoretical capacity compared to graphite. As a result, the Li storage properties of metal oxide anodes have recently been studied extensively.

As a kind of metal oxide anodes, Cu_2O presents some advantages such as abundance, low cost and environment friendly. Nowadays, Cu_2O with different shapes have been regarded as candidate anodes for Li-ion battery studies [13–15]. However, the research enthusiasm on Cu_2O anode materials is far less than that on alloy-typed anodes and even other metal oxide anodes. The main reasons are as follows. Firstly, the theoretical capacity of Cu_2O is relatively low (375 mAh g^{-1}) [15], which is slightly higher than graphite. In this situation, other metal oxides with higher capacity are preferentially selected as research objects. As a result, the studies related to Cu_2O anodes are overlooked. Actually, this weakness can be improved by combining the Cu_2O with some theoretical high-

* Corresponding author.
** Corresponding author.
E-mail addresses: yongguangzhang@hebut.edu.cn (Y. Zhang), clqin@hebut.edu.cn (C. Qin).

https://doi.org/10.1016/j.electacta.2019.01.127
0013-4686/

capacity materials. CoO was introduced by Liu et al. [16] into Cu_2O material. The as-obtained porous CoO/Cu_2O composites presented a reversible capacity of 832 mAh g^{-1} at a current density of 200 mA g^{-1} after 50 cycles. This capacity is double to the theoretical capacity of Cu_2O, indicating that this strategy is effective for further developing Cu_2O anodes with high performance. Secondly, like other metal oxides, Cu_2O also has the characteristic of low conductivity. In order to solve this defect, many scholars have tried to introduce a conductive metal skeleton into active materials to improve the conductivity and rate performance [17]. Wei et al. [15] and Yang et al. [18] adopted solvothermal approach and electrochemical corrosion method respectively to synthesize different Cu_2O nanostructures on Cu foam. These composites presented excellent rate performances. Under this strategy, however, Cu as a skeleton occupies a large mass proportion of the electrode, leading to the ratio of active substance very low. Therefore, the energy density will become low and uncompetitive. In future work, the further reducing of the mass ratio of Cu conductive agent must be considered. Thirdly, metal oxides also have the problem of volume expansion and fracture during the discharge/charge cycling. To remit this problem, porous hollow Cu_2O nanospheres were synthesized and exhibited a capacity of ~650 mAh g^{-1} at 100 mAg^{-1} after 100 cycles [19]. Fu et al. [20] prepared graphene oxide nanosheets wrapped Cu_2O microspheres, it still demonstrated a reversible capacity of 240 mAh g^{-1} at a high current density of 1000 mA g^{-1} after 200 cycles. Thus, nanocrystallization of anode materials with high porosity and encapsulating metal oxides into carbon protective coating are two effective and widely acceptable strategies. Fourthly, the fabrication routes of Cu_2O nanocrystals such as template method and hydrothermal method [14,21,22] are complicated, low yield and expensive. In view of the practical application, it is crucial to develop a large-scale and low-cost synthesis strategy for Cu_2O anodes with desirable performances.

In this study, we develop a new strategy to improve the Li storage performances of Cu_2O anodes. Conductive Cu and theoretical high-capacity GeO_2 dopant were co-introduced into the bimodal porous Cu_2O network by a straightforward dealloying method. During the dealloying process, most of Cu was moderately oxidized into Cu_2O as the main active materials, while a small amount of conductive Cu were maintained and embedded into the Cu_2O network. In the meantime, as a theoretical high-capacity material (1126 mAh g^{-1}) to increase the gross capacity of the anode, a little GeO_2 was also introduced by oxidation of Ge during dealloying process. Furthermore, the as-obtained bimodal porous network provided sufficient room to the volume changes of Cu_2O and GeO_2 materials during discharge/charge cycling. As a result, the material presented a good cycling stability (504 mAh g^{-1} after 150 cycles at 1600 mA g^{-1}) and excellent rate performance as the anode. It's worth mentioning that the strategy adopted in this paper represents three distinct characteristics. Firstly, it provides a large-scale and low-cost synthesis route to obtain Cu_2O-based anode materials. Secondly, it shows a special structural design idea for dealloyed porous materials by utilizing microstructural inheritance from the precursor, which may promote the structural design of various porous metals/metal oxides and the development of the dealloying field. Finally, the strategy can be further applied in future to prepare various porous composite anodes with high capacity for Li-ion battery applications.

2. Experimental methods

$Cu_{17}Ge_{1.3}Al_{81.7}$ master alloy ingots were prepared from pure Cu, Ge and Al (99.99 wt%) ingots (Fig. 1a) by electric arc melting. The master alloy ingots (Fig. 1b) were remelted through induction heating in a quartz tube. Then the melts were sprayed through an orifice onto a copper roller with rotating speed of 2000 r/min. Thus the $Cu_{17}Ge_{1.3}Al_{81.7}$ precursor ribbons (Fig. 1c) were obtained by the so-called melt-spinning method [23,24]. The dealloying of the as-obtained ribbons was treated in a 5 wt% NaOH solution at 25 °C for 20 min, 40 min and 5 h, respectively. During dealloying process, only Al atoms were reacted away while most of Cu atoms reacted with oxygen species at the metallic interface to form Cu_2O network with a small amount of Cu maintained, and the trace Ge elements were oxidized into GeO_2. After dealloying, the outcomes were rinsed through three kinds of liquids for obtaining different metal/metal oxide ratios. For the sample dealloying for 20 min, ultra-pure water (18.2 MΩ cm) was used. Parts of Cu or Cu_2O may further oxidized into CuO by dissolved oxygen in water. For the sample dealloying for 40 min, ultra-pure water and anhydrous ethanol (1:1, volume ratio) was adopted for restraining its further oxidation to a certain degree. For the sample dealloying for 5 h, only anhydrous ethanol was employed for drastically suppressing the oxidation in rinsing process. After dried in vacuum oven at 60 °C for 12 h, the as-designed porous GeO_2/Cu/Cu_2O network was finally obtained (Fig. 1d). A schematic diagram reflecting the fabrication procedure of the experimental samples was presented in Fig. 1.

The phase composition of the dealloying products was confirmed by a Cu Kα X-ray diffractometer (XRD, Bruker, D8-Advance) at 10°/min. The morphology of the network was observed by scanning electron microscope (SEM, Hitachi, S4800) and transmission electron microscope (TEM, JEOL, JEM-2100F). X-ray photo-electron spectroscopy (XPS, ESCALAB 250) was employed to determine the chemical composition and valence state of the products. Brunauer–Emmett–Teller (BET) method was adopted to compare the specific surface area of the different dealloyed products.

The total weight of every dealloying product was considered as the quality of active materials. 70% active material, 20% Ketjen black (conductive additive) and 10% carboxymethyl cellulose (binder) were intermingled in deionized water to form a mixed slurry, then the slurry was blade casted onto Cu foil and dried in vacuum oven at 60 °C for at least 12 h to form the working electrode. The mass loading of the active material was around 0.85 mg cm^{-2}. Celgard 2300 was selected as the separator and lithium foil was used as the counter electrode. $LiPF_6$ (1 M) in mixture of ethylene carbonate (EC) and diethyl carbonate (DEC) (EC:DEC = 1:1, volume ratio) was adopted as the electrolyte. At last, coin cells (CR2025) were assembled in a glove box under Ar protection.

Constant current cycling tests were conducted using a battery cycler system (CT-4008) between 0.01 and 3 V at different current densities. The cyclic voltammetry (CV) test was performed on a Zahner Im6e from 0.01 to 3 V at 0.1 mV s^{-1}. Electrochemical impedance spectroscopy (EIS) analyses were also carried out in the range from 100 kHz to 0.1 Hz.

3. Results and discussion

Dealloying is now one of popular techniques to prepare nanoporous metals and metal oxides [23–26]. Regarding to the Al-Cu alloy system, bicontinuous nanoporous Cu/Cu_2O composites [27] was reported to be synthesized under proper dealloying conditions. In this study, a Al-Cu eutectic alloy composed of Al and Al_2Cu phases [28] is selected as the dealloying precursor. Bimodal porous networks, containing the first class macropores by removal of α-Al as well as the second class micropores and mesopores by etching Al from Al_2Cu phases, can be prepared through microstructural inheritance. With the further extension of the dealloying time, most of Cu was oxidized into Cu_2O. At the same time, Ge was also oxidized and became germanium oxide [29]. In this way, bimodal porous GeO_2/Cu/Cu_2O network was successfully obtained in this

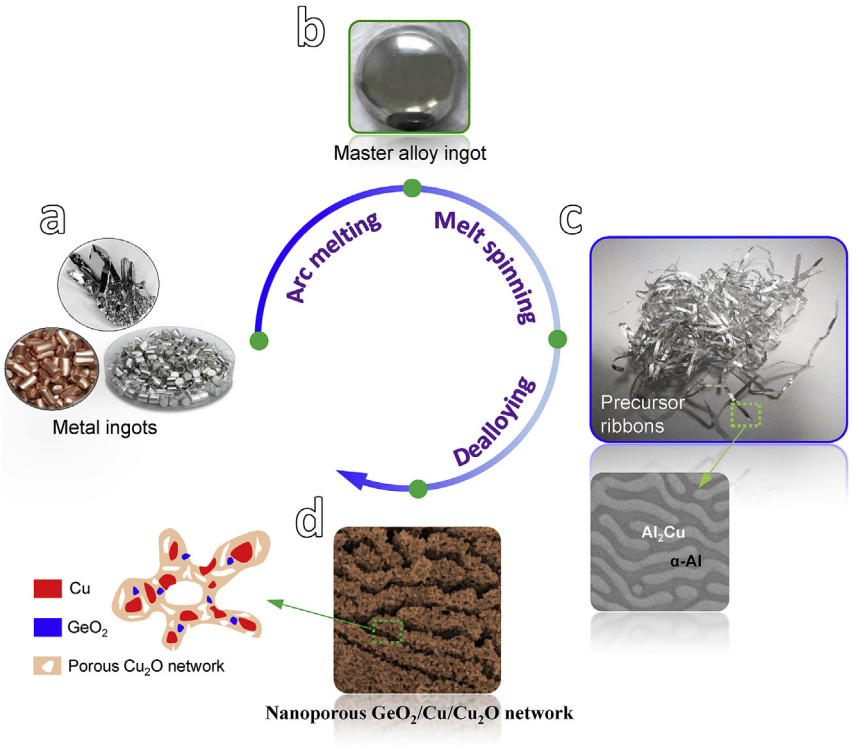

Fig. 1. A schematic diagram showing the fabrication procedure of the experimental samples.

work.

Fig. 2 shows the XRD patterns of the $Cu_{17}Ge_{1.3}Al_{81.7}$ precursor after dealloying for different time. For the sample dealloyed for 20 min, it mainly generates Cu_2O with a small proportion of CuO. For the sample dealloyed for 40 min, only Cu_2O can be detected. Finally, when it dealloyed for 5 h, Cu_2O and a little of Cu appear together. All the peaks in the Fig. 2 can be indexed to crystalline phase CuO (JCPDS No.45-0937), Cu (JCPDS No.65-9743) and Cu_2O (JCPDS No.65-3288). Thus, the XRD result indicates the successful fabrication of the Cu_2O-based materials. Because the atom ratio of Ge is low both in precursor and dealloying product, detectable Ge-related diffraction peaks cannot be found in the XRD results.

TEM images of the $Cu_{17}Ge_{1.3}Al_{81.7}$ alloy after dealloying for different times are shown in Fig. 3. The ligaments of the network

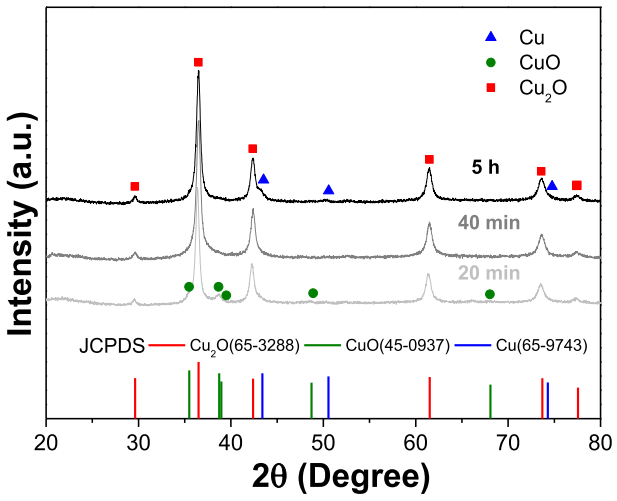

Fig. 2. XRD patterns of the $Cu_{17}Ge_{1.3}Al_{81.7}$ precursor dealloyed for different time.

are clearly and gradually thinning with the extension of the dealloying time. When dealloying for 5 h, the ligaments of the network are only around 55 nm as shown in Fig. 3g, indicating that this corrosion condition resulted in the thinnest materials. The high resolution transmission electron microscope (HRTEM) images are presented in Fig. 3b, e and h. The lattice fringe spacings of 0.232 nm is corresponding to the (111) planes of the CuO phase (Fig. 3b), while in the Fig. 3e, the lattice fringe spacings of 0.245 nm and 0.311 nm can be assigned to the (111) planes of the Cu_2O and (110) planes of the GeO_2 phase respectively. When dealloying for 5 h, well crystallized GeO_2 particles in [001] zone axis direction can be found in Fig. 3h. Furthermore, patterns obtained from the selected area electron diffraction (SAED) confirm that CuO, Cu_2O and GeO_2 exist as shown in Fig. 3c, while Cu_2O, Cu and GeO_2 coexist in Fig. 3f and i. Except the discovery of GeO_2 phase, the results of the HRTEM and SAED mainly corresponds to the results of XRD.

The original $Cu_{17}Ge_{1.3}Al_{81.7}$ precursor ribbons shows a typical microstructure of a eutectic Al-Cu alloy [28], which contains α-Al matrix and Al_2Cu precipitated phase in reticulation form (Fig. 4a). After dealloying for 5 h, a bimodal porous structure (Fig. 4b), containing macropores by removing α-Al from the eutectic microstructure as well as mesopores and micropores by removing Al from Al_2Cu phase, are finally obtained by inheriting original microstructure and selectively etching of Al. The TEM and HRTEM images in Fig. 4c and d disclose that plentiful bumps and particles are formed on the sample surfaces during the dealloying and oxidization process. Moreover, Cu_2O and Cu lattices can be found in Fig. 4d. Thus, GeO_2, Cu_2O and Cu lattice fringes are completely observed in the as-obtained porous network by HRTEM.

The N_2 adsorption/desorption isotherms of the dealloying products can be found in Fig. 4e. The specific surface area of the porous $GeO_2/Cu/Cu_2O$ network dealloyed for 5 h is 86.7 $m^2 g^{-1}$, which is higher than the products dealloyed for 20 min (13.6 $m^2 g^{-1}$) and 40 min (31.29 $m^2 g^{-1}$). The pore size distribution of the three kinds of porous network (Fig. 4f) reveals mesoporous feature

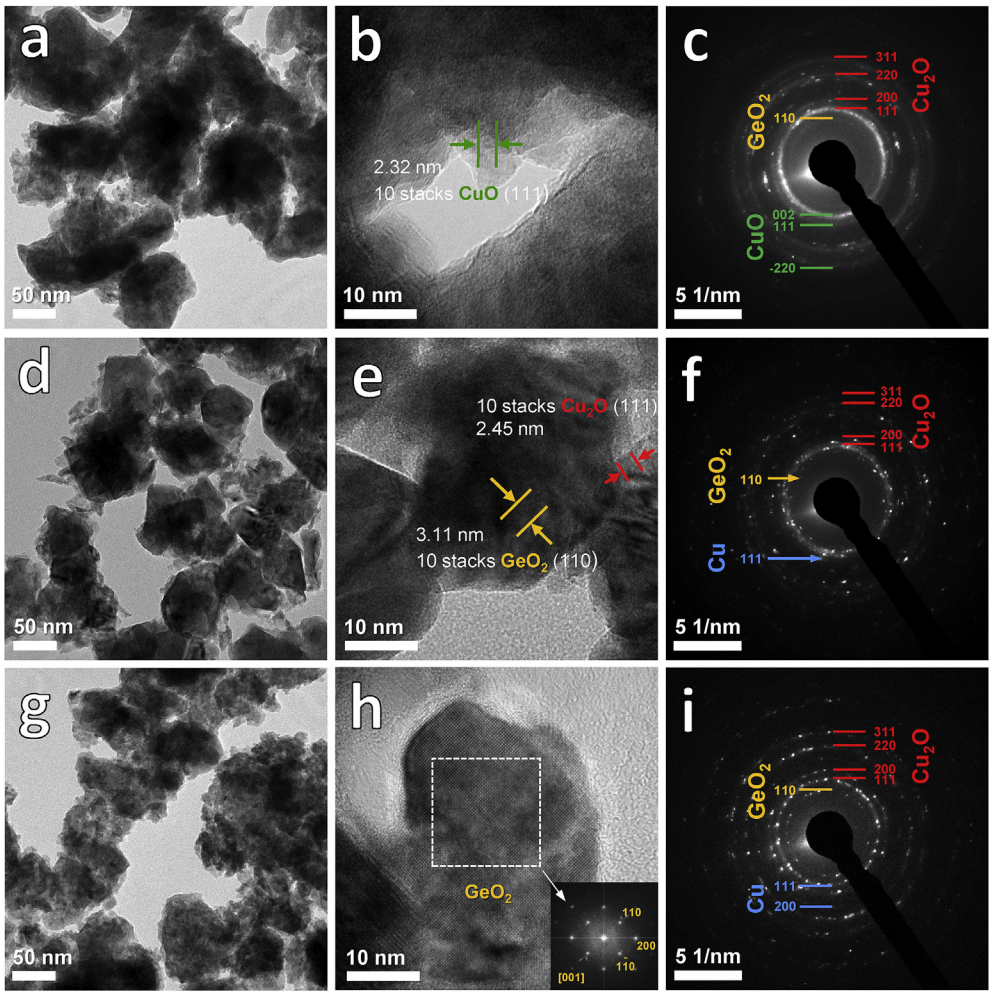

Fig. 3. TEM, HRTEM images and corresponding SAED patterns of the $Cu_{17}Ge_{1.3}Al_{81.7}$ ribbon dealloyed for different time (a–c) 20 min; (d–f) 40 min; (g–i) 5 h.

to a certain degree. In addition, the porous GeO_2/Cu/Cu_2O network shows a biomodal porous characteristic with feature pore sizes locating in the range of 2–6 nm and 20–60 nm respectively, corresponding to the measuring result of pore sizes from the SEM images (Fig. 4b). The presence the biomodal porous features of the network may facilitate electrolyte accessibility and relieve the stress incurred from the volume variations during the repeated discharge/charge cycles.

The XPS measurement, reflecting the chemical components and surface valence states of the dealloying product, is performed and shown in Fig. 5. Fig. 5a presents the full survey spectrum, confirming the presence of Cu, Ge, O and residual Al elements in the final product. Four decomposed peaks at 932.6, 935.1, 952.5 and 955.1 eV (Fig. 5b) can be found in Cu 2p spectrum of the samples. The peaks located at 932.6 and 952.5 eV are corresponding to the Cu $2p_{3/2}$ and Cu $2p_{1/2}$ peaks of Cu_2O [15,30,31]. The characteristic signals at 935.1 (Cu $2p_{3/2}$) and 955.1 eV (Cu $2p_{1/2}$) are attributed to CuO [30,32]. It can be found that with the extension of dealloying time, the area of the peak of Cu_2O increases, which is an indication that the content of Cu_2O is increasing. When the sample dealloyed for 5 h, the majority of the composite is of Cu_2O. Fig. 5c shows the Ge 3d XPS spectra. The main peak contains two deconvoluted peaks at 31.6 and 32.6 eV, corresponding to Ge $3d_{5/2}$ and Ge $3d_{3/2}$ peaks of GeO_2(+4 state) respectively [33,34]. No signals related to Ge(0) state can be tested. This result illustrates that the element Ge is oxidized into GeO_2 during dealloying and spontaneous oxidation process [29]. The O 1s core level spectra (Fig. 5d) includes two deconvoluted peaks, namely at 530.4 and 531.6 eV. The 530.4 eV peak is from the OM oxygen, which corresponds to the −2 oxidation state of the O ions in the metal oxides. The 531.6 eV peak is assigned to OH, which may come from the residual NaOH corrodent [10,35]. These XPS results confirms that when dealloying for 20 min the main superficial product is CuO, while dealloying for 5 h the main superficial product after dealloying changes to Cu_2O.

The final mass ratio (Fig. 6) of different products in three dealloying samples is calculated through combining XPS, EDS and inductively coupled plasma mass spectrometry (ICP-MS) results. It can be seen from Fig. 6 that the main phase composition of samples dealloyed for different time is Cu_2O. With the increase in dealloying time, the mass percent of CuO and Al is declined sharply, and that of GeO_2 is reduced slightly. The content of conductive Cu enhances at the same time. The final mass percent (GeO_2:Cu:Cu_2O:CuO:Al) of the sample dealloyed for 5 h is close to 18.3:10.4:65.1:5.8:0.4, indicating the final product is GeO_2/Cu/Cu_2O composites with small amount of superficial CuO and residual Al.

Fig. 7 shows the first three CV curves of samples dealloying for 20 min, 40 min and 5 h respectively in the potential range of 0.01–3 V at 0.1 mV s^{-1}. The curves for three experimental materials show similar shapes except different peak intensities and slight position offset. It can be found that the area of the CV curves at the second cycle in Fig. 7c is larger than that in Fig. 7a and b, which indicates that the specific capacity of the sample dealloying for 5 h

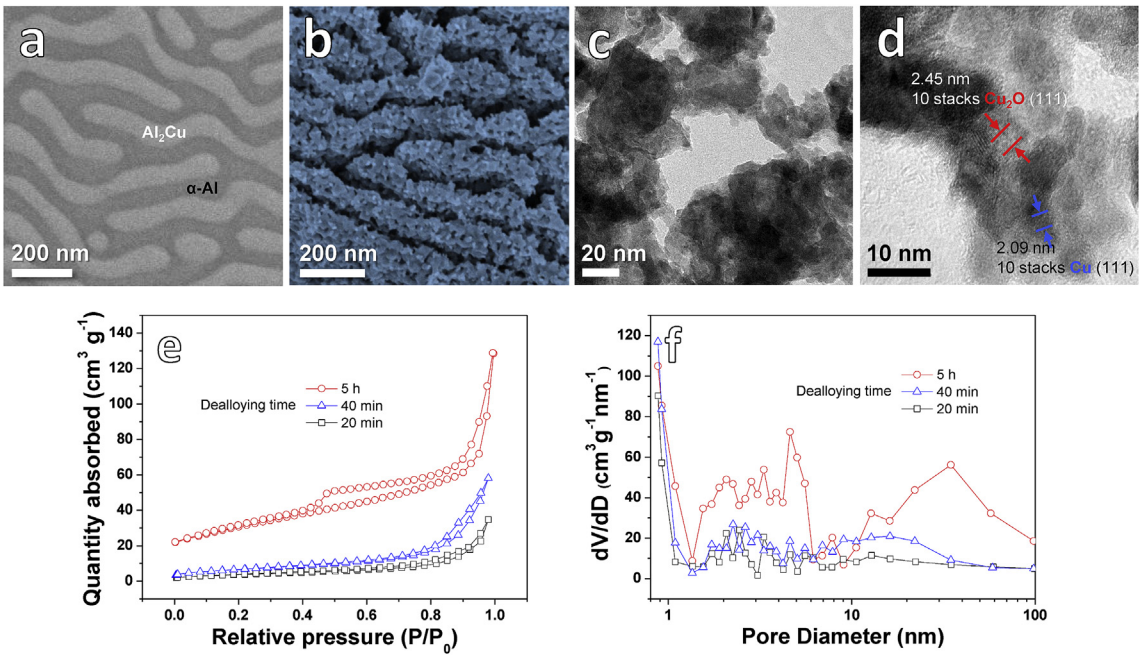

Fig. 4. SEM images of the $Cu_{17}Ge_{1.3}Al_{81.7}$ precursor before (a) and after (b) dealloying for 5 h; (c) and (d) HRTEM images of the $Cu_{17}Ge_{1.3}Al_{81.7}$ ribbon after dealloying for 5 h; (e) Nitrogen adsorption–desorption isotherms of the $Cu_{17}Ge_{1.3}Al_{81.7}$ alloy dealloyed for different time; (f) Pore size distribution curves of the $Cu_{17}Ge_{1.3}Al_{81.7}$ alloy dealloyed for different time.

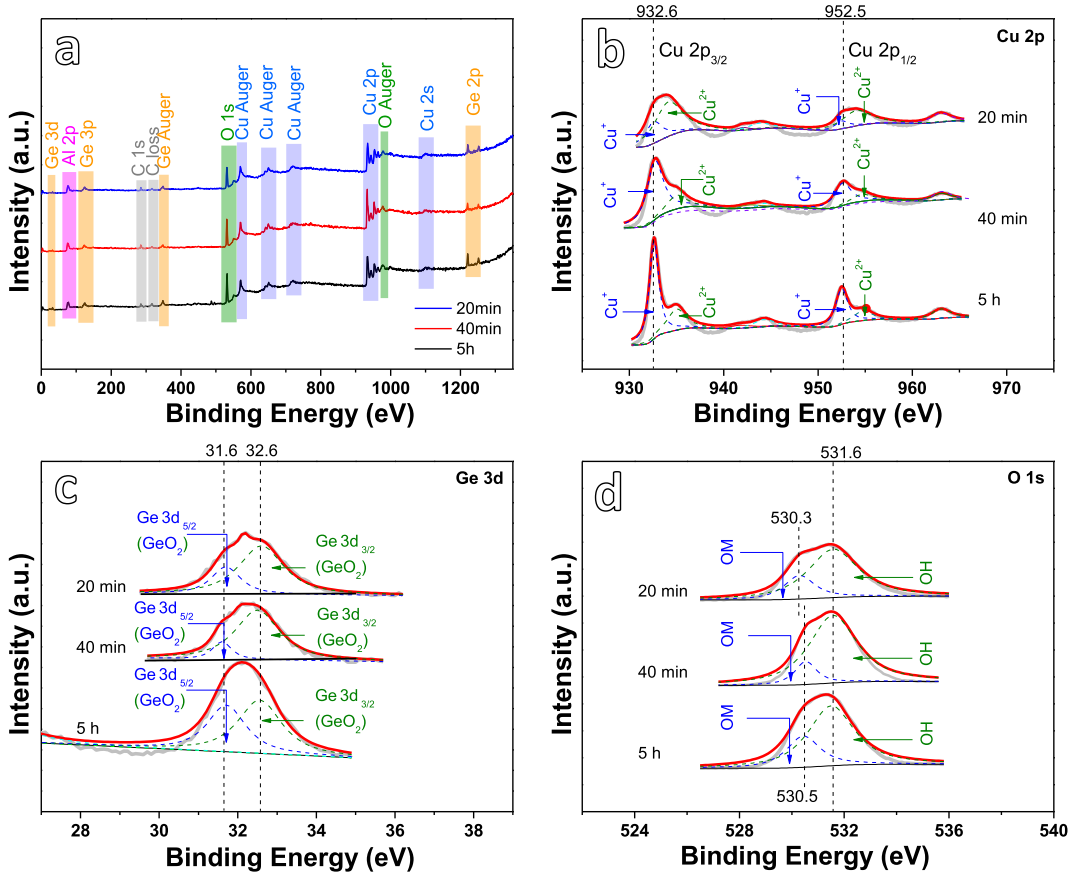

Fig. 5. (a) XPS survey spectra of the $Cu_{17}Ge_{1.3}Al_{81.7}$ alloy dealloyed for different time; High resolution core level spectra of (b) Cu 2p, (c) Ge 3d, (d) O 1s.

after two discharge/charge cycles is higher than the others in this study. In the first cycle, as shown in Fig. 7c, three obvious cathodic peaks located at 1.52 V, 1.1 V and 0.75 V can be found. The peak at 1.52 V is correlated to the Li intercalation reaction into CuO

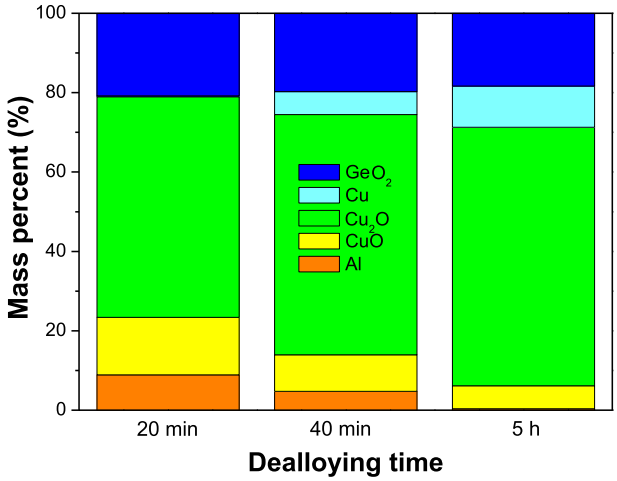

Fig. 6. The mass ratio of different products in the dealloyed samples.

crystallites [36,37] and the formation of Li_xCuO [32]. The peak at 1.1 V and 0.75 V can be assigned to the reduction of CuO to Cu_2O (eq (1)), and the further reduction of Cu_2O to Cu (eq (2)), respectively [38,39]. Furthermore, the wide cathodic peak between 0.4 V and 0.015 V is related to the formation of Ge and Li_2O through deoxidation reaction between GeO_2 and Li (eq (3)), and the formation of Li_xGe in the Li-Ge alloying process (eq (4)) [40]. The above reaction mechanism can be expressed by the following equations (1)–(4) [39,40]:

$$2CuO + 2Li^+ + 2e \rightarrow Cu_2O + Li_2O \quad (1)$$

$$Cu_2O + 2Li^+ + 2e \rightarrow 2Cu + Li_2O \quad (2)$$

$$GeO_2 + 4Li^+ + 4e^- \rightarrow Ge + 2Li_2O \quad (3)$$

$$Ge + 4.4Li^+ + 4.4e^- \rightarrow Li_{4.4}Ge \quad (4)$$

In the anodic scan process, the peak at about 0.54 V corresponds to dealloying of Li_xGe [41–43]. The peak at 1.22 V has been ascertained to be reoxidation of Ge to GeO_2 [41,42], leading to a reversible conversion reaction of GeO_2. Meanwhile, the anodic peaks located at 1.78 V and 2.67 V is attributed to the formation of Cu_2O and CuO, respectively [31,39]. The peak at 1.78 V can be assigned to the oxidation of partial Cu to Cu_2O [39]. The obvious peak at 2.67 V is believed to the further oxidation of Cu_2O to CuO as well as the Li extraction of Cu from the crystal lattice of CuO [14,36]. The initial curve differs markedly from the subsequent two cycles due to the formation of solid electrolyte interphase (SEI) layer [44]. Compared with the first cycle, the peak intensities related to both cathodic and anodic peaks of GeO_2 redox reaction increases observably, this phenomenon implies the gradually improved reversibility of the electrode [45]. While this phenomenon cannot be observed in Fig. 7a and b, demonstrating that the nanoporous network structure and proper ratios among GeO_2, Cu_2O and Cu play important roles in improving the total capacity of the electrode. In the following cycles, the CV curves are very similar in shape expect the reduction peaks shift to higher potentials while no substantial changes are found for the oxidation peaks, which may be ascribed to the structural change of metal oxides after conversion reactions [31,39].

The cycling performance is shown in Fig. 8a at a current density of 200 mA g^{-1} for 50 cycles. It could be found that when the $Cu_{17}Ge_{1.3}Al_{81.7}$ ribbons are dealloyed for 5 h, the discharge capacity of the first cycle reaches to 1097.8 mAh g^{-1} and the charge capacity is 914.2 mAh g^{-1} which represents a loss of about 16.7%. The irreversible capacity loss in the first cycle is mainly due to the formation of the solid electrolyte interphase (SEI) layer. The reversible capacity of the second cycle reduces to 794.4 mAh g^{-1}. After 50 cycles, the reversible capacity still maintains 715 mAh g^{-1}, which shows a good cyclic stability. This good electrochemical property can be attributed to the nanometer effect and synergistic effects among different component materials [30,31,39]. However, when the $Cu_{17}Ge_{1.3}Al_{81.7}$ ribbon dealloyed for 20 min and 40 min, the first discharge capacity is only 436.5 and 585.3 mAh g^{-1} with 26.4% and 20.1% irreversible capacity loss. After 10 cycles, the capacity dropped sharply. The capacity of the samples dealloyed for 20 min and 40 min declines to only 85 and 115 mAh g^{-1} after 50 cycles, showing poor cyclic stabilities. The cycling performance at a high current density of 1600 mA g^{-1} for 150 cycles is shown in Fig. 8b. Even at such a high current density, the first discharge capacity of the anodes which dealloyed for 5 h reached 848.2 mAh g^{-1} and after 150 cycles the capacity of the anode still maintains at 504 mAh g^{-1}, indicating an excellent cyclic stability under high current density. The coulombic efficiency (CE) enhances from 83.5% to 98.7% within 5 cycles, due to the protection of SEI layer for the anode. For latter cycles, the electrode presents high CE above 98% with little fluctuation. However, when the anodes which were dealloyed for 20 min and 40 min run at a high current density of 1600 mAh g^{-1}, only discharge capacity of 129.8 and 150.5 mAh g^{-1} are obtained. After 150 cycles, the capacity remains at a low reversible capacity of 69.2 and 106.9 mAh g^{-1} respectively, showing barely satisfactory cyclic stability and poor reversible capacity under high current density.

Fig. 8c–e shows the constant current charge/discharge curves for the electrodes after 1, 2, 10 and 150 cycles at 1600 mA g^{-1} within a voltage window of 0.01–3 V. For the electrode which was

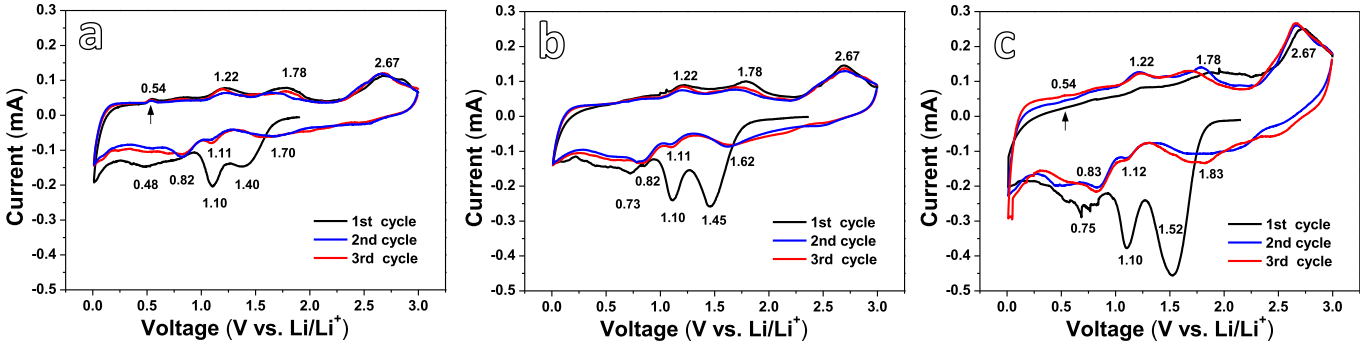

Fig. 7. CV curves of the $Cu_{17}Ge_{1.3}Al_{81.7}$ ribbon dealloyed for different time at a scan rate of 0.1 mV s^{-1} between 0.01 and 3 V: (a) 20 min, (b) 40 min, (c) 5 h.

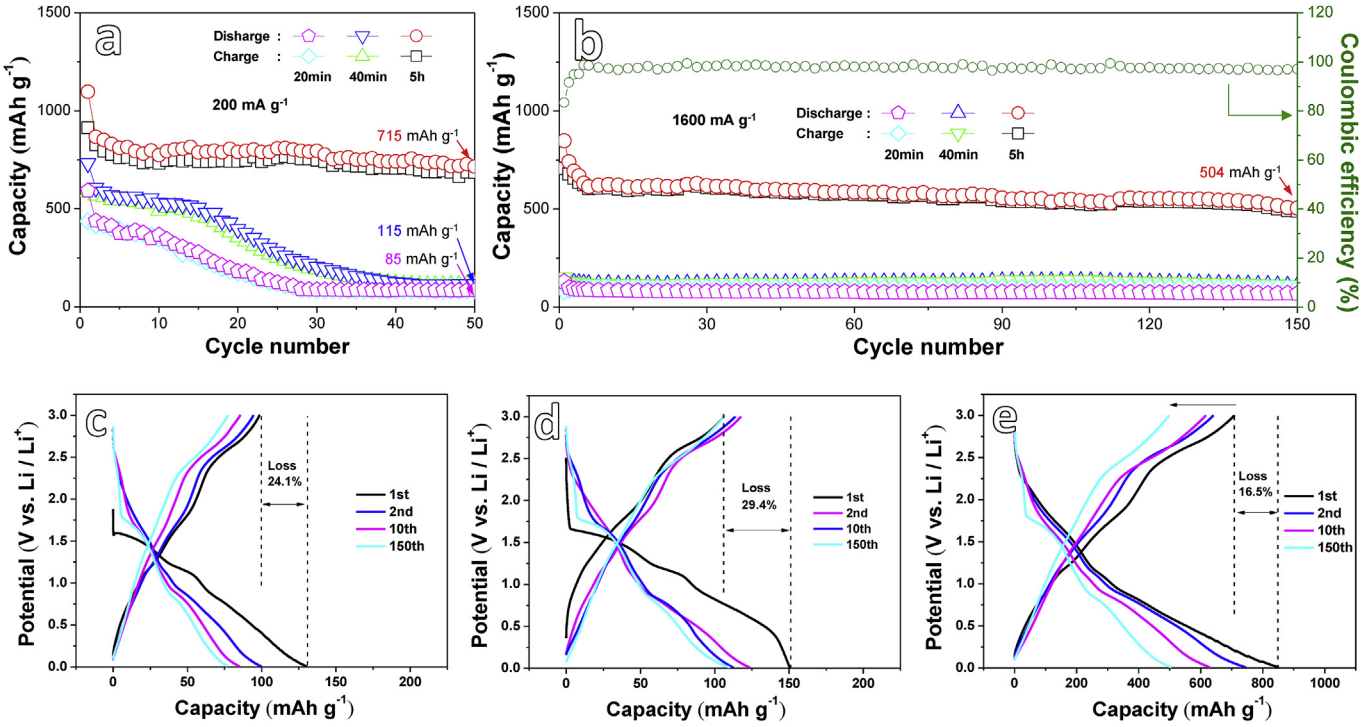

Fig. 8. Cycling performance of the experimental electrodes at a current density of 200 mA g^{-1} (a) and 1600 mA g^{-1} (b); Galvanostatic charge/discharge curves of the experimental samples which were dealloyed for 20 min (c), 40 min (d) and 5 h (e) for the 1st, 2nd, 10th and 150th cycles at a current density of 1600 mA g^{-1}.

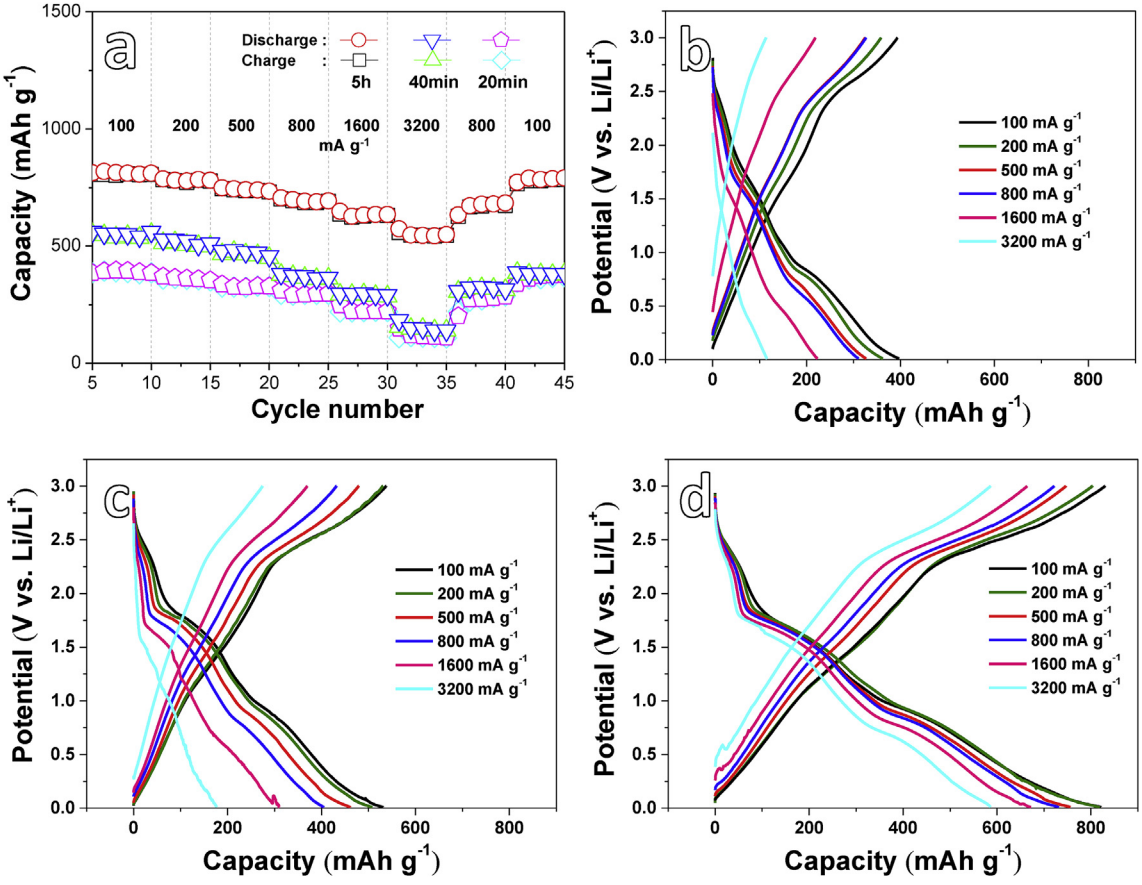

Fig. 9. (a) Rating performances of the experimental anodes tested at different current densities of 100, 200, 500, 800, 1600, 3200, 800 and 100 mA g^{-1}; Typical galvanostatic charge/discharge curves of the experimental samples which were dealloyed for 20 min (b), 40 min (c) and 5 h (d) at current densities of 100, 200, 500, 800, 1600 and 3200 mA g^{-1}.

dealloyed for 5 h (Fig. 8e), four voltage plateaus at 0.3–0.5 V, 0.7–0.9 V, 0.9–1.2 V and 1.4–1.7 V are found in the first discharge step. Meanwhile, four voltage plateaus at 0.4–0.7 V, 1.0–1.3 V, 1.5–1.8 V and 2.2–2.8 V are found in the first charge step. These results are basically accord with CV results. A discharge and charge capacity of 848.2 mAh g^{-1} and 708.5 mAh g^{-1} respectively with an initial CE of 83.5% is obtained from the electrode. With the increase in the cycling number, the curves gradually shift to the left, indicating a slightly decrease in the capacity during cycling. However, the electrode which dealloyed for 20 min (Fig. 8c) delivers a lower discharge and charge capacity of 129.8 mAh g^{-1} and 98.5 mAh g^{-1} respectively with a lower initial CE of 75.9%. The electrode which dealloyed for 40 min (Fig. 8d) also exhibits a lower discharge capacity of 150.5 mAh g^{-1} and a charge capacity of 106.2 mAh g^{-1} with a lower initial CE of 70.6%. So it is obvious that the electrodes dealloyed for 20 and 40 min not only show lower first discharge capacity but also reveal lower initial CE compared with the one dealloyed for 5 h. The above results demonstrate that GeO_2 in porous GeO_2/Cu/Cu_2O network may effectively enhance the electrochemical properties of Cu_2O anodes. Furthermore, although GeO_2 also exists in the electrodes dealloyed for 20 and 40 min, its contribution to capacity is underplay and seems very limited, which could be attributed to the intricate space matching relationship and improper mass ratio among GeO_2, copper and its oxides.

The rate performances of the three electrodes are shown in Fig. 9a, which are evaluated from 100 to 3200 mA g^{-1}. The porous GeO_2/Cu/Cu_2O network electrode which was dealloyed for 5 h delivers capacities of 812, 782, 741, 695, 635 and 552 mAh g^{-1} at current densities of 100, 200, 500, 800, 1600 and 3200 mA g^{-1}, respectively. It is obvious that the porous GeO_2/Cu/Cu_2O network electrode shows higher capacity than other two electrodes at each current density. It should be noted that the capacity recovers to 680 and 791 mAh g^{-1} when the current density is gradually reversed to 800 and 100 mA g^{-1}, which shows great rate performances. However, the electrodes dealloyed for 20 min and 40 min shows poor rate performance and bad reversible capacity under high current density. Fig. 9b–d shows the constant current charge/discharge curves for the three electrodes at different current densities from 100 to 3200 mA g^{-1}. With the increase in the current density, the curves gradually shift to the left, corresponding to the capacity decrease under higher current density. By contrast, the charge/discharge curves of the porous GeO_2/Cu/Cu_2O network electrode shows the best overlap ratio, demonstrating optimal rate performances among the three electrodes further.

Fig. 10a–c shows the microstructure (via SEM) of the three electrode materials after 150 discharge/charge cycles at 1600 mA g^{-1}. The existence of cracks can be clearly found in Fig. 10a and b, showing that serious volume expansion occurred during the cycling. However, no cracks are found in Fig. 10c, indicating that the volume expansion is not obvious during the cycle. These results show that the electrode material dealloyed for 5 h can effectively suppress the volume expansion and ensure its good cycling performance. Fig. 10d and e shows the electrochemical impedance spectroscopy (EIS) of the three electrodes before and after cycling for 150 times at 1600 mA g^{-1}. The semicircles in the high-frequency region reflect the interface charge-transfer process. It could be found that with the extension in the dealloying time, the resistance of the electrodes reduces, which can be ascribed to the increasing conductive Cu content. After 150 cycles, the resistance of the electrode dealloyed for 5 h becomes larger, but is still lower than that of the other two electrodes, indicating a great electrochemical performance. This tendency is consistent with the constant current charge/discharge curves.

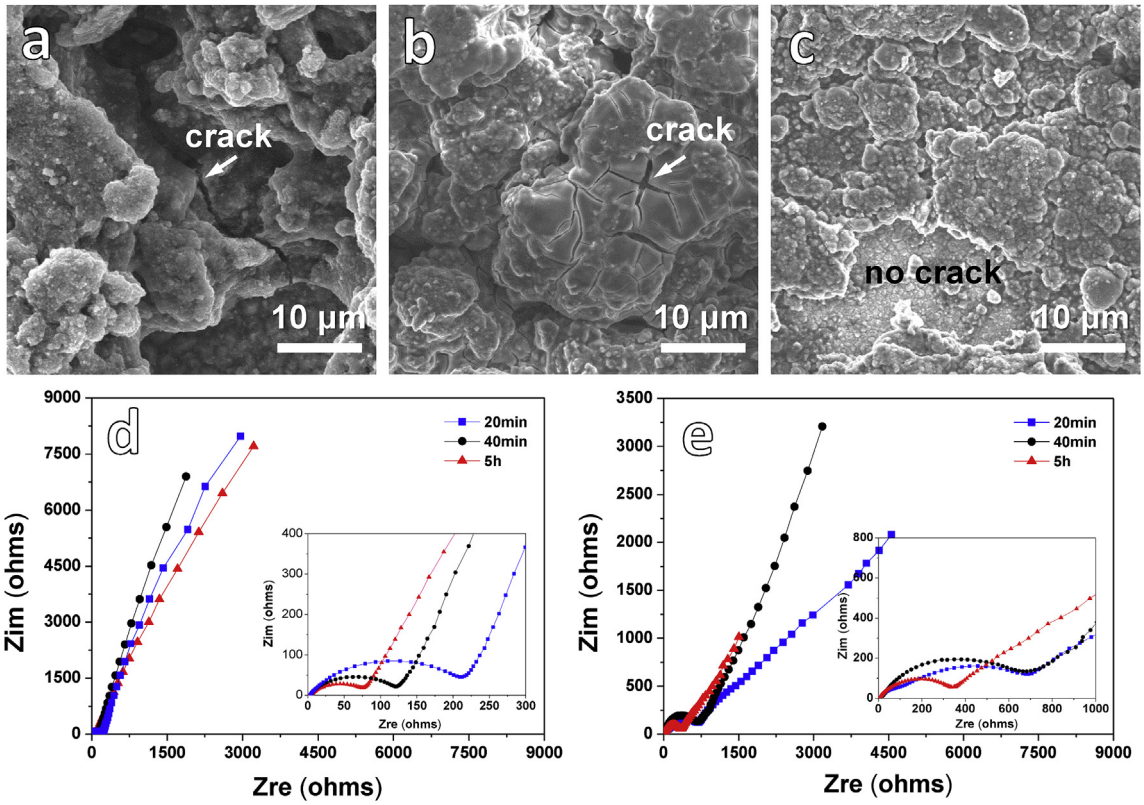

Fig. 10. SEM images of the experimental anodes which were dealloyed for 20 min (a), 40 min (b) and 5 h (c) after cycling for 150 cycles at a current density of 1600 mA g^{-1}; EIS interceptions of the experimental anodes dealloyed for different time at a current density of 1600 mA g^{-1}: (d) fresh, (e) after 150 cycles.

Table 1
The comparison of Li storage performances of Cu_2O-based anodes between this study and the reported literatures.

Anode material	Current density (mA g^{-1})	Cycle number	Reversible capacity (mAh g^{-1})	Reference
Porous Cu_2O/CuO octahedrons	50	50	415	[22]
Cu_2O/CuO/TiO_2 hollow nanocages	50	85	700	[39]
Cu_2O/CuO/Graphitized porous C	60	200	887.3	[31]
Cu_2O-CuO-RGO	100	80	842.5	[30]
Porous hollow Cu_2O nanospheres	100	100	650	[19]
Porous CoO/Cu_2O	200	50	832	[16]
Porous Cu_2O/CuO@CeO_2	200	100	592.3	[46]
Cu_2O/CuO/rGO	337	100	550	[14]
Cu_2O nanorods@Cu foam	400	100	435.1	[15]
Cu_2O/MXene	1000	200	143	[13]
Cu_2O@GO	1000	200	240	[20]
Nanoporous GeO_2/Cu/Cu_2O network	200	50	715	**This work**
	1600	150	504	

The nanoporous GeO_2/Cu/Cu_2O anode exhibits better electrochemical performances than most of the reported literatures, as shown in Table 1 [13–16,19,20,22,30,31,39,46]. The reasons for this good result can be summed up into two aspects. For the componential aspect, there are three favorable factors. Firstly, the addition of GeO_2 greatly improves the gross capacity of electrode. Secondly, the synthesis of Cu in networks increases the conductivity of the electrode and enhances the material's rate performance. Thirdly, the ratio among active material Cu_2O, theoretical high-capacity material GeO_2 and conductive Cu is proper, which guarantees the good capacity and cycling stability. For the structural aspect, there also are three advantageous points. Firstly, the porous network structure provides high surface areas readily accessible by carrier charges and electrolyte, which is beneficial to fast electron and Li-ion transport. Secondly, the plentiful porous network structure can accommodate huge volume variation in repeated charging/discharging cycles, which is helpful for relieving capacity fading. Thirdly, the bimodal porous reticular ligament decreases the Li-ion diffusion distance between the electrode and the electrolyte, and also the diffusion pathway inner the active materials, leading to an improved reaction dynamics. In addition, the strategy used in the paper enriches the structural design idea of dealloying products, which may further promote the development of the dealloying field and could be further applied in future to prepare various porous composite anodes for Li-ion battery applications.

4. Conclusions

We succeeded in preparing a bimodal nanoporous GeO_2/Cu/Cu_2O network as anode materials for Li-ion batteries by a large-scale and low-cost dealloying method. The synergistic effect of porous network and the introduced GeO_2 and Cu can improve the capacity of the anode and alleviate the volume expansion in discharge/charge process effectively, allowing for great cycle and rate performance. The anode delivered a discharge capacity of 715 mAh g^{-1} after 50 cycles at a current density of 200 mA g^{-1}. It still remained a discharge capacity of 504 mAh g^{-1} after 150 cycles at a high current density of 1600 mA g^{-1}. It also exhibited excellent rate performance of 812, 782, 741, 695, 635 and 552 mAh g^{-1} at 100, 200, 500, 800, 1600 and 3200 mA g^{-1} current densities, respectively. When the current density was reversed to 100 mA g^{-1}, it still retained a capacity of 791 mAh g^{-1}. The as-obtained porous Cu_2O-based network was demonstrated to be a promising candidate as anode materials for Li-ion batteries. The paper also revealed a new route on synthesizing other porous composite materials for Li-ion battery applications through the integration of composition and structure design followed by proper dealloying treatment.

Acknowledgements

The authors would like to acknowledge the financial support from the Key Project of Science & Technology Research of Higher Education Institutions of Hebei Province, China (ZD2018059); the China Postdoctoral Science Foundation (2016M600190); the National Natural Science Foundation of China (51671077) and the Program for the Outstanding Young Talents of Hebei Province.

References

[1] K.J. Griffith, K.M. Wiaderek, G. Cibin, L.E. Marbella, C.P. Grey, Niobium tungsten oxides for high-rate lithium-ion energy storage, Nature 559 (2018) 556–563.
[2] T.Y. Lei, W. Chen, W.Q. Lv, J.W. Huang, J. Zhu, J.W. Chu, C.Y. Yan, C.Y. Wu, Y.C. Yan, W.D. He, J. Xiong, Y.R. Li, C.L. Yan, J.B. Goodenough, X.F. Duan, Inhibiting polysulfide shuttling with a graphene composite separator for highly robust lithium-sulfur batteries, Joule 2 (2018) 2091–2104.
[3] W. Chen, T.Y. Lei, W.Q. Lv, Y. Hu, Y.C. Yan, Y. Jiao, W.D. He, Z.H. Li, C.L. Yan, J. Xiong, Atomic interlamellar ion path in high sulfur content lithium-montmorillonite host enables high-rate and stable lithium–sulfur battery, Adv. Mater. 30 (2018), 1804084.
[4] W. Chen, T.Y. Lei, C.Y. Wu, M. Deng, C.H. Gong, K. Hu, Y.C. Ma, L.P. Dai, W.Q. Lv, W.D. He, X.J. Liu, J. Xiong, C.L. Yan, Designing safe electrolyte systems for a high-stability lithium–sulfur battery, Adv. Energy Mater. 8 (2018), 1702348.
[5] W. Chen, T.Y. Lei, T. Qian, W.Q. Lv, W.D. He, C.Y. Wu, X.J. Liu, J. Liu, B. Chen, C.L. Yan, J. Xiong, A new hydrophilic binder enabling strongly anchoring polysulfides for high-performance sulfur electrodes in lithium-sulfur battery, Adv. Energy Mater. 8 (2018), 1702889.
[6] Y.Qi. Li, J.C. Li, X.Y. Lang, Z. Wen, W.T. Zheng, Q. Jiang, Lithium ion breathable electrodes with 3D hierarchical architecture for ultrastable and high-capacity lithium storage, Adv. Funct. Mater. 27 (2017), 1700447.
[7] H.P. Guo, B.Y. Ruan, L.L. Liu, L. Zhang, Z.L. Tao, S.L. Chou, J.Z. Wang, H.K. Liu, Capillary-induced Ge uniformly distributed in N-doped carbon nanotubes with enhanced Li-storage performance, Small 13 (2017), 1700920.
[8] J. Lu, T.P. Wu, K. Amine, State-of-the-art characterization techniques for advanced lithium-ion batteries, Nature Energy 2 (2017) 17011.
[9] G.Y. Zhao, X. Sun, L. Zhang, X. Chen, Y.C. Mao, K.N. Sun, A self-supported metal-organic framework derived Co_3O_4 film prepared by an in-situ electrochemically assistant process as Li ion battery anodes, J. Power Sources 389 (2018) 8–12.
[10] Z.F. Wang, P.Y. Fei, H.Q. Xiong, C.L. Qin, W.M. Zhao, X.Z. Liu, $CoFe_2O_4$ nanoplates synthesized by dealloying method as high performance Li-ion battery anodes, Electrochim. Acta 252 (2017) 295–305.
[11] Y.T. Ma, J. Huang, L. Lin, Q.S. Xie, M.Y. Yan, B.H. Qu, L.S. Wang, L.Q. Mai, D.L. Peng, Self-assembly synthesis of 3D graphene-encapsulated hierarchical Fe_3O_4 nano-flower architecture with high lithium storage capacity and excellent rate capability, J. Power Sources 365 (2017) 98–108.
[12] W.P. Shi, Y.M. Zhang, J.L. Key, P.K. Shen, Three-dimensional graphene sheets with NiO nanobelt outgrowths for enhanced capacity and long term high rate cycling Li-ion battery anode material, J. Power Sources 379 (2018) 362–370.
[13] H. Zhang, H. Dong, X. Zhang, Y.L. Xu, J. Fransaer, Cu_2O hybridized titanium carbide with open conductive frameworks for lithium-ion batteries, Electrochim. Acta 202 (2016) 24–31.
[14] S.H. Wu, G.L. Fu, W.Q. Lv, J.K. Wei, W.J. Chen, H.Q. Yi, M. Gu, X.D. Bai, L. Zhu, C. Tan, Y.C. Liang, G.L. Zhu, J.R. He, X.Q. Wang, K.H.L. Zhang, J. Xiong, W.D. He, A single-step hydrothermal route to 3D hierarchical Cu_2O/CuO/rGO nanosheets as high-performance anode of lithium-ion batteries, Small 14 (2018), 1702667.
[15] W.Q. Chen, W.F. Zhang, L. Chen, L.X. Zeng, M.D. Wei, Facile synthesis of Cu_2O

nanorod arrays on Cu foam as a selfsupporting anode material for lithium ion batteries, J. Alloy. Comp. 723 (2017) 172–178.
[16] T.T. Zhou, Z. Cao, H.Y. Ma, X.Z. Liu, In situ fabrication of hierarchical porous CoO/Cu_2O composites on Cu foam as high-performance freestanding anodes for lithium-ion batteries, Energy Technol. 5 (2017) 1720–1727.
[17] X.Z. Liu, R.E. Zhang, W. Yu, Y.J. Yang, Z.F. Wang, C. Zhang, Y. Bando, D. Golberg, X. Wang, Y. Ding, Three-dimensional electrode with conductive Cu framework for stable and fast Li-ion storage, Energy Storage Mater. 11 (2018) 83–90.
[18] S.B. Ni, X.H. Lv, T. Li, X.L. Yang, L.L. Zhang, Preparation of Cu_2O-Cu anode for high performance Li-ion battery via an electrochemical corrosion method, Electrochim. Acta 109 (2013) 419–425.
[19] S. Prabhakar Rai, A. Sharma, Li-ion storage in morphology tailored porous hollow Cu_2O nanospheres fabricated by Ostwald ripening, RSC Adv. 6 (2016) 105231–105238.
[20] Y.T. Xu, Y. Guo, C. Li, X.Y. Zhou, M.C. Tucker, X.Z. Fu, R. Sun, C.P. Wong, Graphene oxide nano-sheets wrapped Cu_2O micro spheres as improved performance anode materials for lithium ion batteries, Nanomater. Energy 11 (2015) 38–47.
[21] J.Y. Xiang, X.L. Wang, X.H. Xia, L. Zhang, Y. Zhou, S.J. Shi, J.P. Tu, Enhanced high rate properties of ordered porous Cu_2O film as anode for lithium ion batteries, Electrochim. Acta 55 (2010) 4921–4925.
[22] X.J. Zhang, W. Qin, D.S. Li, D. Yan, B.W. Hu, Z. Sun, L.K. Pan, Metal-organic frameworks derived porous CuO/Cu_2O composite hollow octahedrons as high performance anode materials for sodium ion batteries, Chem. Commun. 51 (2015) 16413–16416.
[23] S.Y. Liu, F.J. Pang, Q.W. Zhang, R.J. Guo, Z.F. Wang, Y.C. Wang, W.Q. Zhang, J.Z. Ou, Stable nanoporous Sn/SnO_2 composites for efficient electroreduction of CO_2 to formate over wide potential range, Appl. Mater. Today 13 (2018) 135–143.
[24] D.H. Zheng, F. Zhao, Y.Y. Li, C.L. Qin, J.S. Zhu, Q.F. Hu, Z.F. Wang, A. Inoue, Flexible NiO micro-rods/nanoporous Ni/metallic glass electrode with sandwich structure for high performance supercapacitors, Electrochim. Acta 297 (2019) 767–777.
[25] J.S. Sun, Z. Wen, L.P. Han, Z.W. Chen, X.Y. Lang, Q. Jiang, Nonprecious intermetallic Al_7Cu_4Ni nanocrystals seamlessly integrated in freestanding bimodal nanoporous copper for efficient hydrogen evolution catalysis, Adv. Funct. Mater. 28 (2018), 1706127.
[26] C.X. Xu, R.Y. Wang, Y. Zhang, Y. Ding, A general corrosion route to nanostructured metal oxides, Nanoscale 2 (2010) 906–909.
[27] X.L. Zhang, G.J. Li, S. Yang, X.P. Song, Z.B. Sun, Nanoporous CuO ribbons modified by Au nanoparticles through chemical dealloying and calcination for CO oxidation, Microporous Mesoporous Mater. 226 (2016) 61–70.
[28] M. Okayasu, R. Sato, S. Takasu, Effects of anisotropic microstructure of continuous cast Al–Cu eutectic alloys on their fatigue and tensile properties, Int. J. Fatig. 42 (2012) 45–56.
[29] K.C. Kim, M.Y. Na, W.T. Kim, D.H. Kim, Fabrication of nanoporous GeO_x supported Ag nanoparticle composite by dealloying of $(Al_{0.6}Ge_{0.3}Mn_{0.1})_{98}Ag_2$ amorphous alloy, Corros. Sci. 126 (2017) 381–384.
[30] L.N. Sun, Q.W. Deng, Y.L. Li, L.B. Deng, Y.Y. Wang, X.Z. Ren, P.X. Zhang, Solvothermal synthesis of ternary Cu_2O-CuO-RGO composites as anode materials for high performance lithium-ion batteries, Electrochim. Acta 222 (2016) 1650–1659.
[31] A.Y. Kim, M.K. Kim, K. Cho, J.Y. Woo, Y. Lee, S.H. Han, D. Byun, W. Choi, J.K. Lee, One-step catalytic synthesis of CuO/Cu_2O in a graphitized porous C matrix derived from the Cu-based metal–organic framework for Li and Na-ion batteries, ACS Appl. Mater. Interfac. 8 (2016) 19514–19523.
[32] Z.F. Wang, Y.S. Zhang, H.Q. Xiong, C.L. Qin, W.M. Zhao, X.Z. Liu, Yucca fern shaped CuO nanowires on Cu foam for remitting capacity fading of Li-ion battery anodes, Sci. Rep. 8 (2018) 6530.
[33] A.G. Medvedev, A.A. Mikhaylov, D.A. Grishanov, D.Y.W. Yu, J. Gun, S. Sladkevich, O. Lev, P.V. Prikhodchenko, GeO_2 thin film deposition on graphene oxide by the hydrogen peroxide route: evaluation for lithium-ion battery anode, ACS Appl. Mater. Interfac. 9 (2017) 9152–9160.
[34] W. Wei, F.F. Jia, P. Qu, Z.N. Huang, H. Wang, L. Guo, Morphology memory but reconstructing crystal structure: porous hexagonal GeO_2 nanorods for rechargeable lithium-ion batteries, Nanoscale 9 (2017) 3961–3968.
[35] W.M. Zhao, P.Y. Fei, X.M. Zhang, Y.G. Zhang, C.L. Qin, Z.F. Wang, Porous TiO_2/Fe_2O_3 nanoplate composites prepared by de-alloying method for Li-ion batteriess, Mater. Lett. 211 (2018) 254–257.
[36] L.B. Chen, N. Lu, C.M. Xu, H.C. Yu, T.H. Wang, Electrochemical performance of polycrystalline CuO nanowires as anode material for Li ion batteries, Electrochim. Acta 54 (2009) 4198–4201.
[37] X.P. Gao, J.L. Bao, G.L. Pan, H.Y. Zhu, P.X. Huang, F. Wu, D.Y. Song, Preparation and electrochemical performance of polycrystalline and single crystalline CuO nanorods as anode materials for Li ion battery, J. Phys. Chem. B 108 (2004) 5547–5551.
[38] P. Subalakshmi, A. Sivashanmugam, CuO nano hexagons, an efficient energy storage material for Li-ion battery application, J. Alloy. Comp. 690 (2017) 523–531.
[39] G.X. Wang, Y.M. Sui, M.N. Zhang, M. Xu, Q.X. Zeng, C. Liu, X.M. Liu, F. Du, B. Zou, One-pot synthesis of uniform Cu_2O-CuO-TiO_2 hollow nanocages and highly stable lithium storage properties, J. Mater. Chem. 5 (2017) 18577–18584.
[40] X. He, Y. Hu, Z. Shen, R.Z. Chen, K.S. Wu, Z.L. Cheng, X.W. Zhang, P. Pan, Channelized carbon nanofiber with uniform-dispersed GeO_2 as anode for long-lifespan lithium-ion batteries, J. Alloy. Comp. 729 (2017) 313–322.
[41] J.H. Zhang, T.T. Yu, J.L. Chen, H.L. Liu, D.Q. Su, Z.H. Tang, J.F. Xie, L. Chen, A.H. Yuan, Q.H. Kong, Germanium-based complex derived porous GeO_2 nanoparticles for building high performance Li-ion batteries, Ceram. Int. 44 (2018) 1127–1133.
[42] F. Panto, Y.F. Fan, S. Stelitano, E. Fazio, S. Patane, P. Frontera, P. Antonucci, N. Pinna, S. Santangelo, Electrospun C/GeO_2 paper-like electrodes for flexible Li-ion batteries, Int. J. Hydrogen Energy 42 (2017) 28102–28112.
[43] X.N. Li, J.W. Liang, Z.G. Hou, Y.C. Zhu, Y. Wang, Y.T. Qian, Coordination complex pyrolyzation for the synthesis of nanostructured GeO_2 with high lithium storage properties, Chem. Commun. 50 (2014) 13956.
[44] R. Xu, S.P. Wu, Y. Du, Z. Zhang, A facile route to dually protected Ge@GeO_2 composites as anode materials for lithium ion battery, Chem. Eng. J. 296 (2016) 349–355.
[45] W. Wei, H. Wang, A.H. Tian, K.F. Wang, J.M. Wang, P. Qu, S.Y. Zhang, L. Guo, Confined metal Ge quantum dots in carbon nanofibers for stable rechargeable batteries, Nanoscale 10 (2018) 6872–6877.
[46] L.J. Wang, X.J. Wang, Z.H. Meng, H.J. Hou, B.K. Chen, MOF-templated thermolysis for porous CuO/Cu_2O@CeO_2 anode material of lithium-ion batteries with high rate performance, J. Mater. Sci. 52 (2017) 7140–7148.